Ocean Engineering 216 (2020) 108098

Contents lists available at ScienceDirect

Ocean Engineering

journal homepage: www.elsevier.com/locate/oceaneng

Properties of breaking irregular waves over slopes

Ankit Aggarwal [a,*], Mayilvahanan Alagan Chella [a,c], Hans Bihs [a], Dag Myrhaug [b]

[a] Department of Civil and Environmental Engineering, Norwegian University of Science and Technology, Trondheim, Norway
[b] Department of Marine Technology, Norwegian University of Science and Technology, Trondheim, Norway
[c] Earth Sciences University of Notre Dame, Indiana, USA

ARTICLE INFO

Keywords:
Geometric properties
Irregular wave breaking
Wave deformation
Submerged bar

ABSTRACT

The present study numerically investigates the breaking and spectral characteristics and geometric properties of breaking irregular waves over slopes for different incident waves. The growth of wave non-linearity and wave energy redistribution during shoaling and breaking process are observed to be major factors in determining the free surface elevation skewness and spectral bandwidth. In general, the variation of the breaker indices with the surf similarity parameter is found to be mainly governed by the type of wave breakers. The wave breaker type further depends on the seabed slope, incident wave parameters and water depth at the location of wave breaking. The study further explores the geometric properties for both spilling and plunging irregular wave breakers. The wave deformation due to wave-seabed interaction plays a major role in affecting the breaker shapes. Every individual breaking wave in the irregular wave train possesses different wave profiles and breaker characteristics. In order to study these parameters in a probabilistic way, the statistics of the breaker characteristics and the breaker shape parameters are investigated. The lognormal distribution is noticed to be the most suitable fit for the wave crest steepness and asymmetry factors. This study is performed using the open-source computational fluid dynamics (CFD) based numerical model. The numerical model is validated for a submerged bar under breaking irregular waves and the numerical results are compared with experimental data. The transformations of the free surface elevation due to wave shoaling, wave breaking and wave decomposition are explored.

1. Introduction

During the last few decades, considerable efforts have been made to study wave breaking in the coastal regions. Wave breaking primarily governs the various hydrodynamic processes in the surf zone like destabilization of the sea bed, wave setup and wave energy dissipation. A lot of research has been dedicated in the past towards the wave hydrodynamics investigation of breaking regular waves (Goda, 1970; Hwang, 1984; Weggel, 1972; Camenen and Larson, 2007). Their studies revealed many important parameters to quantify and understand the regular wave breaking process. However, the study of breaking regular waves is not sufficient to describe and investigate the real sea state. The real sea state is highly irregular and composed of many harmonic wave components. In contrast to regular waves, there is no well defined breaking point for irregular waves. The breaking location is different for each individual wave component depending on the individual wave steepness. Therefore, the energy dissipation of irregular waves occurs over a larger surf zone area in comparison to regular waves. The breaker type also varies for each wave component of an irregular wave train. The breaking characteristics and the geometric properties of discrete breaking events in the irregular wave train are distinct from each other due to the different amplitudes and frequencies. The hydrodynamics of breaking irregular waves are still not fully understood and are relatively uncertain. When the beach slope is constant, the temporal and spatial variability of wave breaking should solely depend on the incident wave spectrum (Ting, 2001).

Some researchers have attempted to investigate the individual wave breaking frequency and statistics of breaking irregular waves. A field study was conducted by Thorpe and Humphries (1980) to study the relationship between the mean frequency of wave breaking at a fixed point and the average distance between irregular breaking waves. The wavelet method has been used analytically to determine and quantify the breaking statistics by Mori and Yasuda (1994) and Liu (2000). Their study revealed that the surface jumps associated with the breaking waves can be well detected in the wavelet spectra. Ochi et al. (1996) investigated the joint probability distribution of wave excursion and the associated time interval of non-narrow-banded random process. They showed that the breaking probability depends on the shape of the wave spectrum for deep water waves. Seyama and Kimura (1988)

* Corresponding author.
E-mail address: hans.bihs@ntnu.no (H. Bihs).

https://doi.org/10.1016/j.oceaneng.2020.108098
Received 21 January 2020; Received in revised form 25 August 2020; Accepted 10 September 2020
Available online 16 September 2020

measured the properties of breaking irregular waves over a slope. They concluded that the shoaling property of zero-down-cross waves can be approximated by linear wave theory. Also, the wave properties during the breaking process and after breaking differ considerably from those for periodic waves. Beji and Battjes (1993) studied the irregular wave propagation over a submerged bar experimentally and further investigated wave breaking and wave shoaling under irregular waves for different spectral wave steepnesses. Ting (2001) explored the wave and turbulence characteristics of broad- and narrow-banded irregular waves over a sloping sea bed. They also reported the probability distributions for the wave height and peak velocities for the breaking irregular waves. Kjeldsen and Myrhaug (1978) conducted a study to investigate the geometric properties of breaking waves. A wave crest deformation can be observed both horizontally and vertically at the onset of wave breaking.

Several numerical and analytical studies have been performed to investigate breaking regular waves. The numerical studies of non-linear surface waves have been conducted in the past by using potential flow theory (Watson and West, 1975; Longuet-Higgins and Cokelet, 1976). Chen et al. (1999) reported that this approach is unable to capture the complete breaking process accurately. The assumptions in the potential flow theory are valid up to the breaking point; these assumptions become invalid at the onset of wave breaking. The detailed information about the flow properties for the free surface flows can be computed by Computational Fluid Dynamics (CFD). In order to capture the complete breaking process, CFD can be used without defining any empirical breaking criterion explicitly. A number of CFD investigations have been carried out to study breaking regular waves (Lin and Liu, 1998; Bradford, 2000). The turbulence scales in their simulations were represented with the turbulence models. Many studies were also performed using two-phase models to investigate breaking waves, since two-phase models give a more realistic representation of the wave breaking process (Hieu et al., 2004; Garcia et al., 2004; Christensen, 2006; Lara et al., 2006). The detailed reviews on the previous work with CFD modelling for breaking waves can be found in Lara et al. (2006), Bradford (2000) and Hieu et al. (2004). Alagan Chella et al. (2015, 2016) studied the breaking characteristics and geometric properties of breaking regular waves over slopes using a CFD based model. They compared the numerical results with experimental data by Ting and Kirby (1996). The numerical results showed good agreement with the experimental data for free surface elevation, horizontal and vertical velocities and turbulent kinetic energy. Paulsen et al. (2013) simulated non-breaking irregular waves using CFD to study the wave loads on monopile structures. However, there is limited literature available for breaking irregular waves propagating over slopes in shallow waters. There are only a few studies performed in the past to investigate the transformations in the parameters like free surface elevation skewness, spectral bandwidth, breaking characteristics and geometric wave profile properties during the breaking process for irregular waves in shallow water over slopes. Due to the complex phenomena involved during wave breaking, most of the studies involving breaking irregular waves are limited to field and laboratory experiments. Already developed and tested approaches like CFD modelling can be used to investigate these less explored aspects of breaking irregular waves over slopes.

The objective of the present paper is to numerically investigate breaking irregular waves over slopes in the time- and frequency-domains and to analyse the transformations in the free surface elevation skewness, spectral bandwidth, breaking characteristics and wave crest profile during the wave propagation over slopes. The previous studies related to breaking irregular waves in shallow water have not been focused on addressing these aspects in detail. The breaking characteristics of irregular waves are relatively complex to study as there is no clearly defined breaking point and no clear distinction between the different breaker types. The regular wave breaking characteristics have been relatively well studied in the past (Alagan Chella et al., 2015, 2016). The present study includes the investigation of the breaking and spectral characteristics of irregular waves. The energy transfer from the spectral peak region towards higher-frequencies during the wave shoaling and wave breaking processes is quantified by using the method used by Tian et al. (2011) for breaking focused wave groups. Further, the analysis of the geometric properties of irregular wave breakers is performed for different breaker types to explore the role of seabed slope and incident wave parameters in the wave breaking process. Many numerical and experimental studies have been carried out in the past to study the geometric properties of regular breaking waves, but only a few studies exist which have addressed the geometric properties of irregular wave breakers. To the best of the authors' knowledge, the present study is the first attempt to investigate these parameters for breaking irregular waves over slopes.

The numerical simulations are conducted using a CFD based two-phase numerical model REEF3D (Bihs et al., 2016; Bihs and Kamath, 2017). This model has been successfully used to investigate different coastal and marine engineering problems (Afzal et al., 2015; Ong et al., 2017; Aggarwal et al., 2019a,b, 2020; Afzal et al., 2020). The numerical model employs higher-order numerical schemes capable of capturing the complete breaking process. The validation for modelling of breaking irregular waves is performed by comparing the numerical results for breaking irregular waves over a submerged bar with the experiments performed by Beji and Battjes (1993) during the complex transformation processes like wave shoaling and wave breaking. Next, the propagation of irregular breaking waves over sloping seabeds is investigated. The wave energy transfer from the spectral peak region towards the different frequency ranges, breaking wave statistics and the changes in free surface elevation skewness and spectral bandwidth during the breaking process are studied in detail. An extensive analysis to explore the breaking wave characteristics and the geometric properties for different cases is performed. The wave crest steepness and asymmetry parameters are examined in order to understand the influence of water depth and incident wave steepness in determining the deformation in the wave crest. The statistics of breaking wave characteristics and geometric properties of the breakers are also analysed and discussed to quantify these parameters.

2. Numerical model

2.1. Governing equations

The present study is performed using a CFD based numerical model REEF3D (Bihs et al., 2016; Bihs and Kamath, 2017). The Reynolds-Averaged Navier–Stokes equations (RANS) are defined with the assumption of an incompressible fluid. The momentum conservation equation together with the continuity equation define the Navier–Stokes equations:

$$\frac{\partial u_i}{\partial x_i} = 0 \tag{1}$$

$$\frac{\partial u_i}{\partial t} + u_j \frac{\partial u_i}{\partial x_j} = -\frac{1}{\rho}\frac{\partial P}{\partial x_i} + \frac{\partial}{\partial x_j}\left[(\nu + \nu_t)\left(\frac{\partial u_i}{\partial x_j} + \frac{\partial u_j}{\partial x_i}\right)\right] + g_i \tag{2}$$

where u is the velocity averaged over time t, ρ is the fluid density, P is the pressure, ν is the kinematic viscosity, ν_t is the eddy viscosity, i and j denote the indices in x and y direction, respectively, and g_i is the acceleration due to gravity.

The solution for the pressure in the Navier–Stokes equations is obtained from the projection method (Chorin, 1968). The Poisson pressure equation is solved with the HYPRE integrated conjugate gradient solver preconditioned with geometric multigrid (Falgout and Yang, 2002). The fifth-order finite difference Weighted Essentially Non-Oscillatory (WENO) scheme in multi-space dimensions is utilized in the present study (Jiang and Shu, 1996). The third-order TVD Runge Kutta scheme is applied for the time discretization (Shu and Oscher, 1988). The viscous terms are source term dependent and result in very low CFL

numbers when discretized explicitly. In order to avoid this, the viscous terms are treated with an implicit method to take it out of the CFL criterion. Adaptive time stepping is used in order to control the time-step size based on the CFL number (Griebel et al., 1998). The numerical model utilizes a Cartesian grid in order to use higher-order discretization schemes. The present study uses the $k-\omega$ model used to calculate the eddy-viscosity by solving for the turbulent kinetic energy k and the specific turbulent dissipation ω (Wilcox, 1994):

$$\frac{\partial k}{\partial t} + u_j \frac{\partial k}{\partial x_j} = \frac{\partial}{\partial x_j}\left[\left(\nu + \frac{\nu_t}{\sigma_k}\right)\frac{\partial k}{\partial x_j}\right] + P_k - \beta_k k\omega \tag{3}$$

$$\frac{\partial \omega}{\partial t} + u_j \frac{\partial \omega}{\partial x_j} = \frac{\partial}{\partial x_j}\left[\left(\nu + \frac{\nu_t}{\sigma_\omega}\right)\frac{\partial \omega}{\partial x_j}\right] + \frac{\omega}{k}\alpha P_k - \beta\omega^2 \tag{4}$$

where P_k is the turbulent production rate and is defined as follows:

$$P_k = \nu_t \frac{\partial u_i}{\partial x_j}\left[\frac{\partial u_i}{\partial x_j} + \frac{\partial u_j}{\partial x_i}\right] \tag{5}$$

The other closure coefficients are $\alpha = \frac{5}{9}$, $\beta_k = \frac{9}{100}$, $\beta = \frac{3}{40}$, $\sigma_\omega = 2$, $\sigma_k = 2$. The over-production of the turbulence in highly strained flow associated with the oscillatory fluid motion under waves outside the boundary layer is prevented by limiting the eddy-viscosity (Durbin, 2009) as follows:

$$\nu_t = \min\left(\frac{k}{\omega}, \sqrt{\frac{2}{3}}\frac{k}{|\mathbf{S}|}\right) \tag{6}$$

where $\mathbf{S}$ is the mean rate of strain.

In the present study, the level set method (Osher and Sethian, 1988) is implemented to capture the free surface. The level set function gives the closest distance to the interface and the two phases are distinguished by the change of the sign. The function can be written as:

$$\phi(\vec{x},t)\begin{cases} > 0 & if\ \ \vec{x} \text{ is in phase 1} \\ = 0 & if\ \ \vec{x} \text{ is at the interface} \\ < 0 & if\ \ \vec{x} \text{ is in phase 2} \end{cases} \tag{7}$$

2.2. Irregular wave generation

The relaxation method is utilized for the wave generation and absorption (Mayer et al., 1998). The values for the velocities and the free surface are ramped up from the computational values to the ones obtained from wave theory. Also, the reflected waves which travel back towards the inlet are absorbed with this method. A numerical beach is needed at the end of the wave flume in order to dissipate waves and avoid reflections. In the relaxation method, a smooth transition is made from the computational solution to the still water conditions. The irregular waves are composed of the super-positioning of regular wave components. The first-order irregular waves are generated by summation of the linear regular waves components. The free surface η is defined as:

$$\eta = \sum_{i=1}^{N} A_i cos\theta_i \tag{8}$$

$$A_i = \sqrt{2S(\omega_i)\Delta\omega_i} \tag{9}$$

$$\theta_i = k_i x - \omega_i t + \epsilon_i \tag{10}$$

$$\omega_i^2 = g k_i \tanh k_i h \tag{11}$$

where N is the number of components, A_i is the amplitude of each wave component, $S(\omega_i)$ is the spectral density and θ_i is the phase, ϵ_i is a random number rectangularly distributed between 0 and 2π, ω_i is the angular frequency, λ_i is the wavelength and k_i is the wave number ($k_i = \frac{2\pi}{\lambda_i}$).

Similarly, the wave-induced horizontal velocity u and the wave-induced vertical velocity w are computed as the sum of the individual u and w components in the irregular wave train. The second-order irregular wave theory given by Dalzell (1999) which takes into account the second-order wave–wave interaction is used for the higher spectral wave steepness cases:

$$\eta = \eta_1 + \eta_2 \quad ; \qquad u = u_1 + u_2 \quad ; \qquad w = w_1 + w_2 \tag{12}$$

where η_1, u_1 and w_1 represent the first-order components and η_2, u_2 and w_2 represent the second-order components (the details of the second-order irregular wave theory can be found in Dalzell (1999)).

In the present study, the Joint North Sea Wave Project (JONSWAP) spectrum is used for the generation of irregular waves (Hasselmann et al., 1980). The waves propagating close to the coast are usually fetch-limited and are never fully developed. The required significant wave height H_s, the peak angular frequency ω_p and number of components N are given as input values to the JONSWAP spectrum. The frequency spectrum $S(\omega)$ gives the distribution of the wave energy with angular frequency ω.

$$S(\omega) = \frac{5}{16} H_s^2 \omega_p^4 \omega^{-5} exp\{\frac{-5}{4}(\frac{\omega}{\omega_p})^{-4}\}\gamma^{exp\{\frac{-(\omega-\omega_p)^2}{2\sigma^2\omega_p^2}\}} A_\gamma \tag{13}$$

where $\gamma = 3.3$; $A_\gamma = 1$ - 0.287 ln (γ); $\sigma = 0.07$, when $\omega < \omega_p$; $\sigma = 0.09$, when $\omega > \omega_p$

2.3. Validation of the numerical model for breaking irregular waves over a submerged bar

The numerical model is validated for breaking irregular waves over an impermeable submerged bar by comparing the numerical results with the experiments by Beji and Battjes (1993). In the experimental setup, the length of the wave flume is 37.70 m, the width is 0.8 m and the height is 0.75 m. The still water level over the horizontal bottom is $d = 0.4$ m. In the experiments, a piston type wavemaker was used for generating irregular waves based on the JONSWAP spectrum. A submerged trapezoidal bar with a weather side slope of 1:20 and a 2 m long horizontal crest followed by a 1:10 lee side slope was installed at a distance of $x = 6$ m from the wavemaker. Eight wave gauges were installed along the length of the wave flume in the experimental setup to measure the free surface elevation. A two-dimensional numerical wave tank is used to simulate the experiments described above. The numerical setup including the wave gauge locations is illustrated in Fig. 1.

The numerical tests are performed for the grid convergence study with input $H_s = 0.054$ m and the spectral peak period $T_p = \frac{2\pi}{\omega_p} = 2.5$ s for four different uniform grid sizes $dx = 0.10$ m, 0.05 m, 0.01 m and 0.005 m for the wave gauge located at $x = 11$ m. Fig. 2 presents the comparison of experimental and numerical spectral wave density at $x = 11$ m with $dx = 0.10$ m (total number of mesh elements = 3440), 0.05 m (total number of mesh elements = 13 760), $dx = 0.01$ m (total number of mesh elements = 344 000), and $dx = 0.005$ m (total number of mesh elements = 1.38 million). The wall time (simulation time) is around 3 h with $dx = 0.10$ m, 12 h with $dx = 0.05$ m, 120 h for case with $dx = 0.01$ m and 230 h for case with $dx = 0.005$ m. The simulations are performed to obtain 200 s of the flow data. Furthermore, 128 processors are used for the present simulations. The computations are conducted on the supercomputer which is based on the Intel Xeon E5-2670 processor with 2.6 GHz speed and a memory of 2 GB per core. The present simulations employ the Cartesian grid approach, which means that the grid size is uniform in both directions for a 2D wave tank (dx = dy). The spectral densities S_η are normalized by the total spectral density at WG1 (x = 6 m). It is observed that the numerical results with $dx = 0.10$ m and 0.05 m underestimate the peak spectral density by 45% and 26%, respectively. Also, the spectral density in the higher frequency range (0.75 Hz–2.0 Hz) is not correctly represented. This is due to the insufficient number of cells per wavelength. The difference between the peak experimental and numerical spectral wave

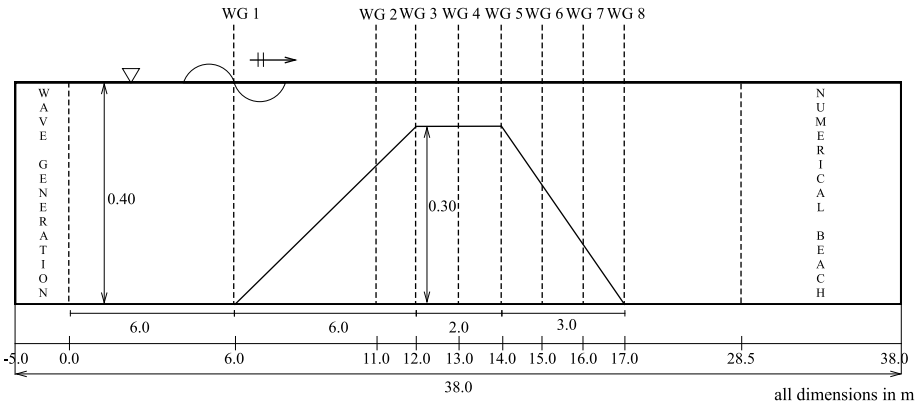

Fig. 1. Numerical setup with the wave gauge positions for a submerged bar in the numerical wave tank.

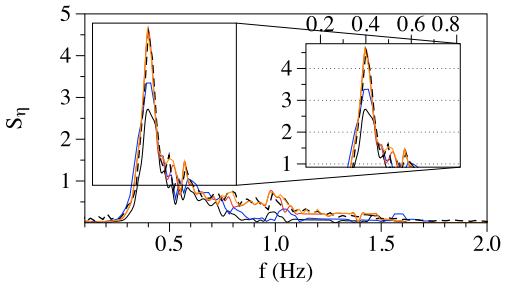

Fig. 2. Comparison between the numerical results and the experimental data (a) Grid convergence study for the wave gauge located at x = 11 m. Red line for experiments; orange line for dx = 0.005 m; dashed black line for dx = 0.01 m; blue line for dx = 0.05 m; solid black line for dx = 0.10 m. (For interpretation of the references to colour in this figure legend, the reader is referred to the web version of this article.)

density reduces to 3% and the spectral wave density at all frequencies is represented with a reasonable accuracy with dx = 0.01 m and 0.005 m. The increase in accuracy on changing dx from 0.01 m to 0.005 m is not very significant, but the computational costs increase by almost a factor of 2. Thus, dx = 0.01 m is chosen for the further simulations. The reduction in the spectral density is due to the loss of energy during the wave breaking process. For the wave gauges located on the downslope, a large reduction in incident spectral density is observed because most of the waves in the irregular wave train have already broken and a large amount of the wave energy has already been dissipated during the breaking and redistributed during the wave decomposition process. Fig. 3 presents the comparison of S_η for the wave surface elevations at the six different wave gauge locations x = 11 m, 12 m, 13 m, 15 m, 16 m and 17 m with dx = 0.01 m.

Correlation coefficient (R) (Van Loco et al., 2002) is also calculated to compare numerical and experimental spectral wave densities. R can have a maximum value of 1 and it would mean a perfect correlation. The spectral peak and energy distributions are well represented for WG2 at x = 11 m with R = 0.997 (Fig. 3a). A major portion of the spectral density lies between the frequency range from 0 to 1.5 Hz. At x = 12 m (WG3), the still water depth is reduced to its minimum value resulting in further shoaling and the value of R is 0.993 (Fig. 3b). The peak value of the spectrum is slightly reduced and the wave spectrum becomes broader (0 Hz to 2 Hz) as compared to the spectrum for the previous wave gauge location (0 Hz to 1.7 Hz). This is due the increasing contribution of the wave energy of the shorter waves, as can be expected during the shoaling process. This observation is consistent with the experiments. Fig. 3c shows the results at x = 13 m (WG4) and has R = 0.992. At this location, many waves in the wave train have already broken and the peak of the spectrum is further reduced. The contribution of wave energy towards higher frequencies is further increased. The wave gauge located at x = 15 m (WG6, on the lee side slope of the bar) indicates further reduction of the spectrum with energy transfer towards higher frequencies with R = 0.995 (Fig. 3d). This is caused by the wave decomposition process attributed to the increasing water depth on the lee side of the slope (Kamath et al., 2017). The waves are decomposed into secondary and tertiary components, visible through the multiple peaks at the higher frequencies in the wave spectrum. The total energy spectral density of the wave train is also considerably reduced (Figs. 3e with R = 0.993 and 3f with R = 0.992); the redistribution of the wave energy takes place and the energy from the primary peak is transferred towards the secondary and tertiary peaks at the higher frequencies. The size of the sampling interval for FFT and the spectral smoothening process might be the reason for some irregularities in the wave spectra.

3. Breaking irregular waves over impermeable slopes

Alagan Chella et al. (2015, 2016) have performed a numerical study on the breaking of regular waves and compared their numerical results with the experiments by Ting and Kirby (1996). The present investigation focuses on breaking irregular waves over slopes. The setup used in the present study is similar to that of Ting and Kirby (1996). The spectral wave steepness s for the irregular waves is defined as:

$$s = \frac{2\pi H_{so}}{gT_p^2} \tag{14}$$

where, H_{so} is the offshore significant wave height and T_p is the spectral peak period.

The breaking of regular waves can be defined by four types: spilling, plunging, collapsing and surging depending on the surf similarity parameter. The surf similarity parameter at breaking (ξ_b) is a function of the wave steepness at breaking (s_b) and the slope of the seabed (m) (Battjes, 1974).

$$\xi_b = \frac{m}{\sqrt{s_b}}; s_b = \frac{2\pi H_b}{gT^2} \tag{15}$$

$$\begin{cases} \xi_b < 0.4 & \text{Spilling} \\ 0.4 < \xi_b < 2.0 & \text{Plunging} \\ \xi_b > 2.0 & \text{Surging or Collapsing} \end{cases} \tag{16}$$

The spectral surf similarity parameter (ξ) is defined as a function of the spectral wave steepness (s) and the slope of the seabed (m).

$$\xi = \frac{m}{\sqrt{s}} \tag{17}$$

The breaker depth index (γ_b) and breaker height index (Ω_b) are two parameters used to investigate the breaking characteristics of waves.

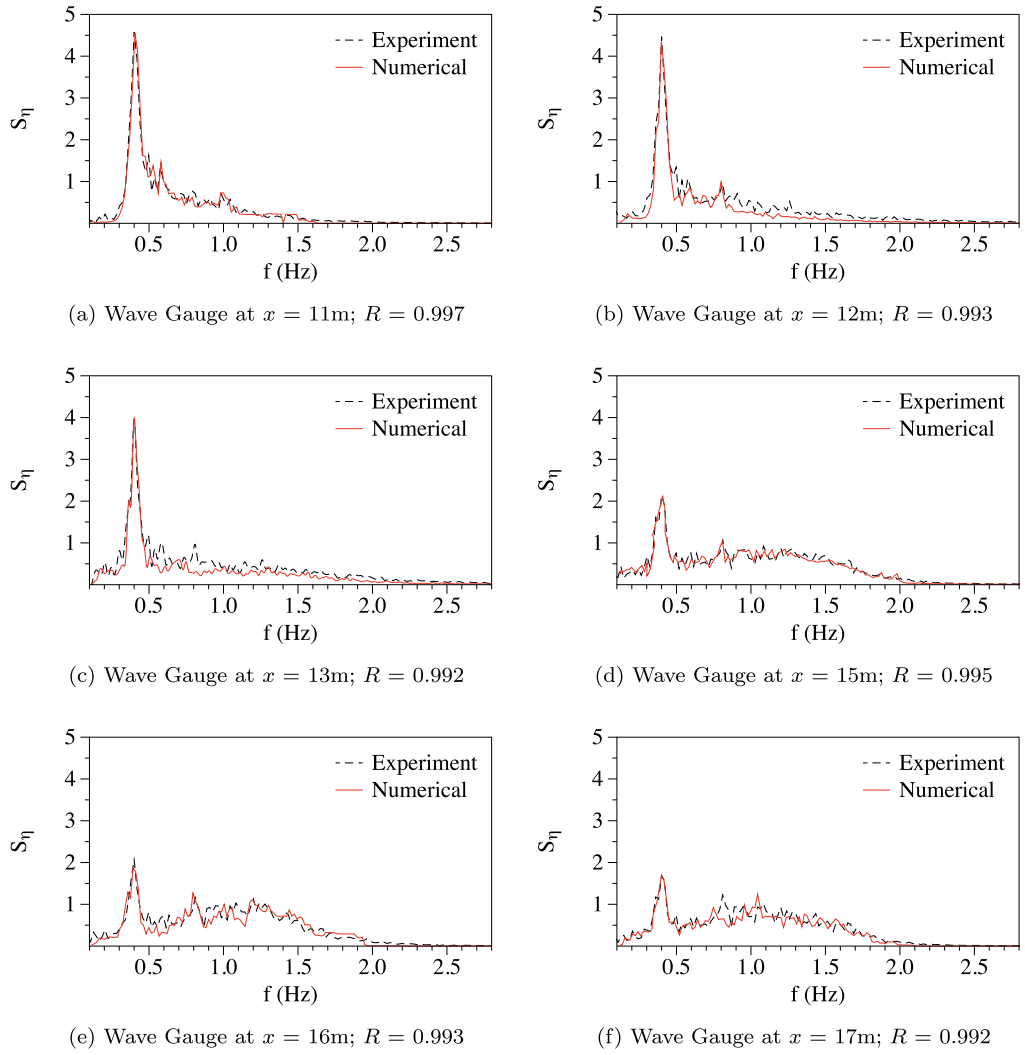

(a) Wave Gauge at $x = 11$m; $R = 0.997$

(b) Wave Gauge at $x = 12$m; $R = 0.993$

(c) Wave Gauge at $x = 13$m; $R = 0.992$

(d) Wave Gauge at $x = 15$m; $R = 0.995$

(e) Wave Gauge at $x = 16$m; $R = 0.993$

(f) Wave Gauge at $x = 17$m; $R = 0.992$

Fig. 3. Comparison of numerical and experimental spectral wave density for $dx = 0.01$ m at different wave gauge locations.

They are defined as:

$$\gamma_b = \frac{H_b}{d_b}; \Omega_b = \frac{H_b}{H_{so}} \tag{18}$$

where, d_b is the depth at breaking, T is the zero-crossing period of individual waves at breaking, H_b is the local wave height at breaking and H_{so} is the offshore significant wave height.

Kjeldsen and Myrhaug (1978) defined the steepness and asymmetry parameters for the local wave crest asymmetry at breaking: the wave crest front steepness (ε), the wave crest rear steepness (δ), the horizontal asymmetry factor (μ) and the vertical asymmetry factor (λ). The present study uses these steepness and asymmetry parameters to study the geometric properties of breaking irregular waves over different slopes.

3.1. Computational setup and test cases

The two-dimensional numerical wave tank is 20.5 m long and 1 m high as shown in Fig. 4. The water depth is $d = 0.4$ m. The wave breaking is prominently influenced by the spectral steepness of the incident wave spectrum and the slope of the seabed. The numerical simulations are performed for three different seabed slopes $m = 1/25$, $1/35$ and $1/45$. Wave spectra with four different wave steepnesses $s = 0.0142$, 0.0267, 0.0445 and 0.0623 are tested on each slope. Therefore, an investigation of 12 different cases in total is performed (Table 1). All simulations are run for $t = 200$ s with the number of wave components $N = 499$. Nine wave gauges are placed along the numerical wave tank. The distance of the wave gauge (x) is measured from the toe of the slope (Fig. 4 for $m = 1{:}35$). The locations of the wave gauges are changed with each change in slope, i.e. becoming more crowded together for the 1:25 slope, and L_s is the length of the slope which shortens and is different with the increasing slope value (m). Occurrence of wave breaking, changes in the spectral characteristics and the wave transformations are analysed and presented for all 12 cases. Further, the study investigates the energy level evolution, the breaker characteristics and the geometric properties of breaking irregular waves over slopes. In order to demonstrate the effect of environmental parameters on the breaking characteristics, two different scenarios are presented in more detail: the wave spectrum with lower spectral steepness on a steeper slope (case A1) and the wave spectrum with higher spectral steepness on a milder slope (case C4).

3.2. Wave transformation

3.2.1. Irregular wave breaking process

When the irregular wave train approaches the shore, the wave height, wave length and the energy content of each wave component change as the water depth decreases. The wave length becomes shorter as the wave height and wave energy increase due to the shoaling process. This process continues until the fluid particle velocity exceeds the wave crest velocity which leads to wave breaking. Fig. 5 presents the computed free surface profile with velocity variations during the

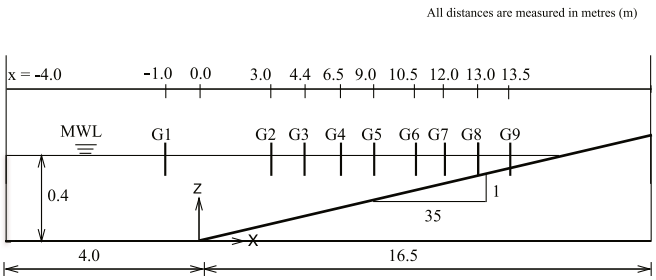

Fig. 4. Setup of the numerical wave tank used in the study (Side view and representing the setup for simulations with slope m = 1:35 and slope length L_s = 16.5 m).

Table 1
Simulation cases for study of wave propagation over impermeable slope.

Sim. No.	Slope m	H_{so} (m)	T_p (s)	Spectral steepness s	Spectral surf similarity parameter ξ
A1	1:25	0.032	1.2	0.0142	0.3357
A2		0.06	1.2	0.0267	0.2448
A3		0.10	1.2	0.0445	0.1896
A4		0.14	1.2	0.0623	0.1602
B1	1:35	0.032	1.2	0.0142	0.2398
B2		0.06	1.2	0.0267	0.1748
B3		0.10	1.2	0.0445	0.1354
B4		0.14	1.2	0.0623	0.1145
C1	1:45	0.032	1.2	0.0142	0.1865
C2		0.06	1.2	0.0267	0.1360
C3		0.10	1.2	0.0445	0.1053
C4		0.14	1.2	0.0623	0.0890

wave propagation over the slope at t = 52.7 s, 52.9 s, 53.05 s, 53.2 s, 53.27 s and 53.39 s, respectively. When the waves propagate over the slope, they undergo shoaling which is observed by the increase in wave crest heights. As the waves propagate further over the slope, the main wave crest becomes almost vertical which denotes the onset of wave breaking as can be seen in Fig. 5a. The wave breaking is embarked by the small water jet at the wave crest. The profile of the wave crest becomes highly deformed and asymmetric. When the fluid particle velocity at the wave crest exceeds the wave celerity, an over-turning motion of the wave crest is induced (Fig. 5b). The overturning wave crest breaks with an encasement of an air pocket (Fig. 5c), referred to as the splash-up phenomenon and generates another small jet of water in the downstream direction (Figs. 5d, 5e, 5f). The results for the wave profile deformation during the breaking process are consistent with previous studies (Lubin et al., 2006; Christensen, 2006; Alagan Chella et al., 2016).

Fig. 6 presents the distribution of the normalized significant wave height (H_s/H_{so}) versus the normalized distance along the wave tank (x/L_s) for (a) cases A1–A4 with m = 1:25 (b) cases B1–B4 with m = 1:35 and (c) cases C1–C4 with m = 1:45, where L_s is the length of the slope (in the order of the lower to the upper symbols in Fig. 6). For a given slope, the waves with lower spectral wave steepness s undergo more shoaling and have a higher value of H_s/H_{so} in the breaking zone compared to the waves with higher spectral wave steepness s. For case A4 (s = 0.0623, m = 1:25), the wave height becomes $1.29H_{so}$ in contrast to case A1, where the wave height is $1.37H_{so}$ in the breaking zone. As expected, the wave breaking zone (around which most of the waves in the irregular wave train break, i.e. x/L_s) shifts farther offshore as the spectral wave steepness increases for a given slope. The waves with larger s lose most of the incident wave energy when they reach shallower water depths due to the breaking at relatively deeper depths. The waves with lower s contain relatively more energy when they approach shallower water depths and thus, a higher value of H_s/H_{so} (in comparison with the waves with larger s), and the breaking zone is relatively more onshore.

3.2.2. Energy level evolution

This section demonstrates the energy transfer between the different frequency ranges of the wave spectrum by tracking the wave energy levels at different frequency ranges during the wave shoaling and wave breaking processes. Five different frequency ranges of the wave spectrum are considered: spectral peak region (f/f_p = 0.9–1.1, E_1), above-peak region (f/f_p = 1.2–1.5, E_2), higher-frequency region (f/f_p = 1.5–2.5, E_3), low frequency range (0.5–0.9, E_4), significantly high frequency region (2.5–5, E_5) and total energy E ($E_1 + E_2 + E_3 + E_4 + E_5$). This is similar to the methodology used by Tian et al. (2011) to investigate the energy transfer for breaking focused wave groups. These energy levels are non-dimensionalized with the total incident wave energy E_{0m}. Fig. 7 presents the variation of the energy levels at different frequency ranges versus the normalized distance in the NWT. For case A1 (s = 0.0142, $m2$ = 1:25), as the waves propagate over the slope, the energy levels from the spectral peak region E_1 and low frequency range E_4 are slightly reduced due to wave shoaling, and this energy is transferred to the above-peak region E_2 as noticed by an increase in E_2 (Fig. 7a). The energy levels during the wave shoaling process in the higher-frequency region E_3 and the significantly high frequency region E_5 remain almost constant. After breaking, the energy from the

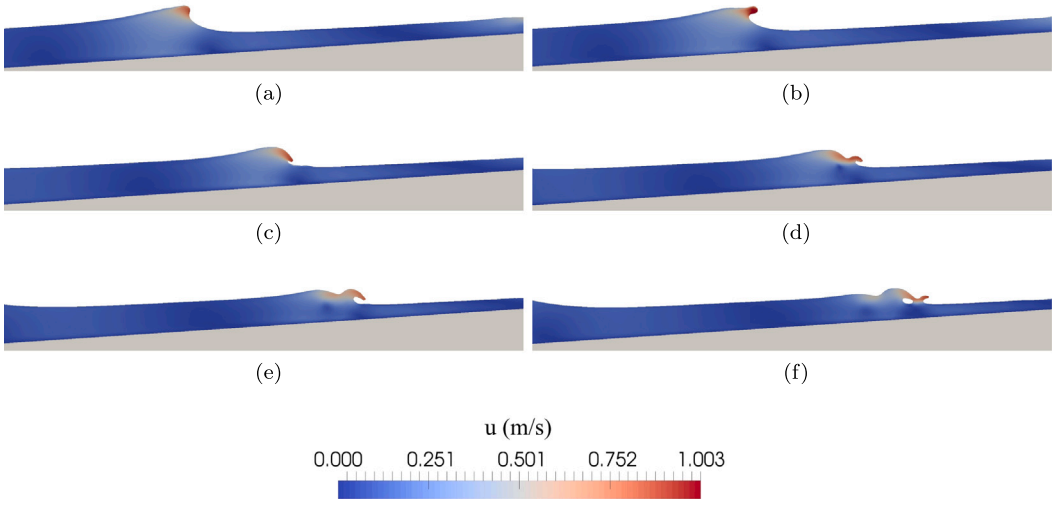

Fig. 5. Computed wave profile with the horizontal velocity variation (m/s) during the wave propagation over sloping seabed (case B4) at t = (a) 52.7 s (b) 52.9 s (c) 53.05 s (d) 53.2 s (e) 53.27 s (f) 53.39 s.

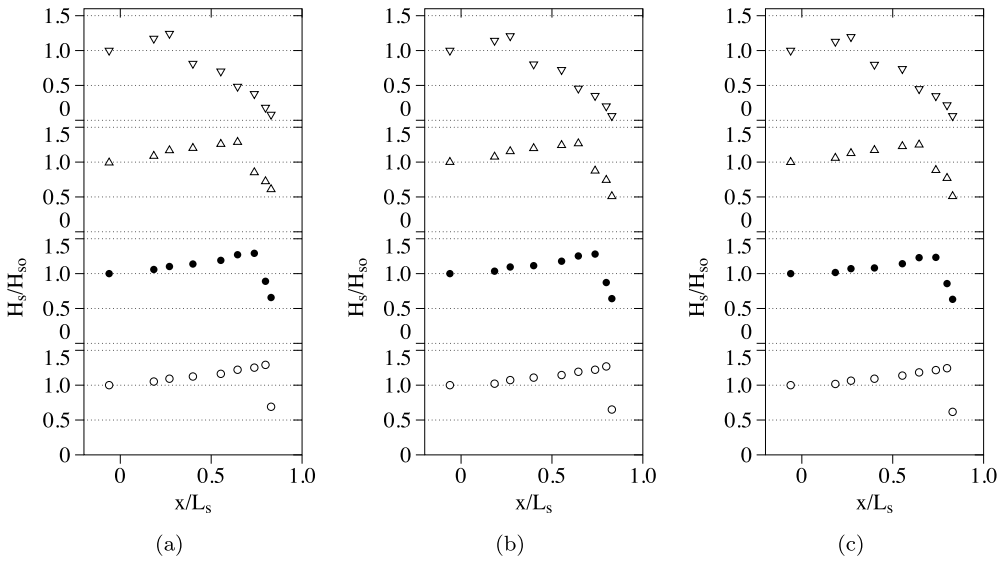

Fig. 6. Variation of the normalized significant wave height versus the normalized distance for different steepnesses for m = (a) 1:25 (cases A1–A4); (b) 1:35 (cases B1–B4); (c) 1:45 (cases C1–C4). Open circles represent s = 0.0142; black circles for s = 0.0267; triangles for s = 0.0445; inverted triangles for s = 0.0623.

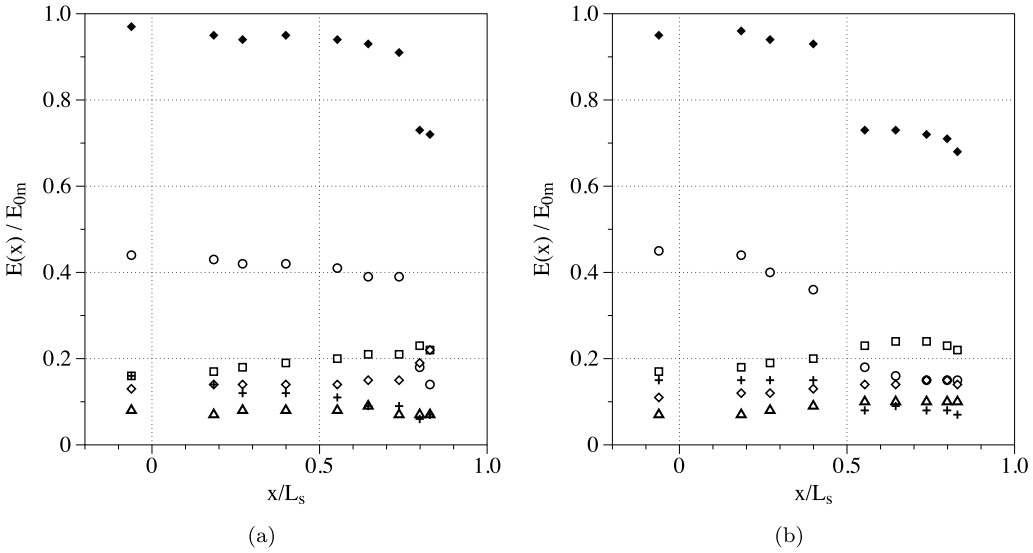

Fig. 7. Variation of the energy levels versus the normalized distance in NWT for (a) case A1 (s = 0.0142, m = 1:25); (b) case C4 (s = 0.0623, m = 1:45). Open circles represent $E_1(x)/E_{0m}$; squares represent $E_2(x)/E_{0m}$; white rhombus represent $E_3(x)/E_{0m}$; plus represent $E_4(x)/E_{0m}$; triangles represent $E_5(x)/E_{0m}$; dark rhombus represent $E(x)/E_{0m}$.

spectral peak region is significantly reduced (54%). This is due to the energy dissipation during breaking and energy transfer towards E_2 and E_3, as noticed by the increase in their energy levels after breaking. The energy levels in the significantly high frequency range E_5 are not affected much. For case C4, a similar behaviour is observed (Fig. 7b). However, the wave breaking occurs at larger water depths for this case, due to which the energy dissipation from the spectral peak E_1 for case C4 occurs earlier and some of the energy is transferred to the higher-frequencies in E_2 and E_3.

3.2.3. Free surface elevation skewness and spectral bandwidth

The skewness and kurtosis of the free surface elevation η measures the deviation from the linear theory with reference to the mean η value. The skewness β and kurtosis are defined respectively, as (Goda, 2010):

$$\beta = \frac{1}{\eta_{rms}^3}\frac{1}{N}\sum_{i=1}^{N}(\eta_i - \bar{\eta})^3 \tag{19}$$

$$Kurtosis = \frac{1}{\eta_{rms}^4}\frac{1}{N}\sum_{i=1}^{N}(\eta_i - \bar{\eta})^4 . - 3 \tag{20}$$

where $\bar{\eta}$ is the mean value and η_{rms} is the rms (root-mean-square) value.

The bandwidth of the spectrum ν quantifies the broadness or narrowness of the spectrum (Longuet-Higgins, 1975):

$$\nu^2 = \frac{m_0 m_2}{m_1^2} - 1 \tag{21}$$

where, m_n is the spectral moment defined as:

$$m_n = \int_0^\infty \omega^n S(\omega) d\omega; n = 0, 1, 2... \tag{22}$$

Fig. 8 presents the distribution of the skewness (β) along the wave tank (x/L_s) for (a) cases A1–A4 with m = 1:25, (b) cases B1–B4 with m = 1:35, and (c) cases C1–C4 with m = 1:45 (in the order of the lower to the upper symbols in Fig. 8). An increase in β is observed in the shoaling zone and a decreasing trend is noticed inside the surf zone (the surf zone starts from the location of wave breaking and extends till the beach). The values of β for cases A4 (s = 0.0623, m = 1:25) and C4 (s = 0.0623, m = 1:45) are 0.87 and 0.84, respectively at the breaking point. After breaking, the skewness value is reduced to β = 0.52 for case A4

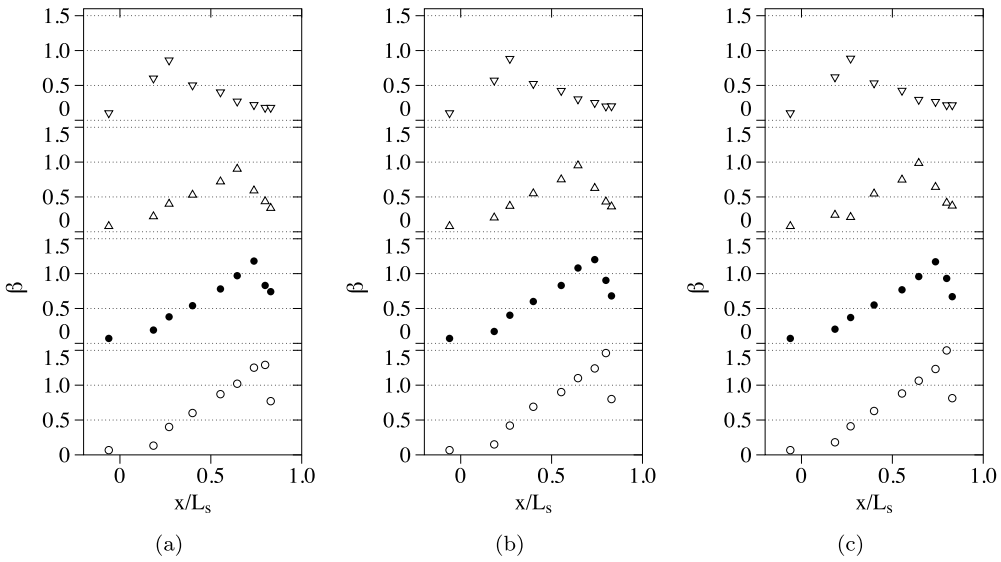

Fig. 8. Variation of the skewness versus the normalized distance in NWT for different steepnesses for m = (a) 1:25 (cases A1–A4); (b) 1:35 (cases B1–B4); (c) 1:45 (cases C1–C4). Open circles represent s = 0.0142; black circles for s = 0.0267; triangles for s = 0.0445; inverted triangles for s = 0.0623.

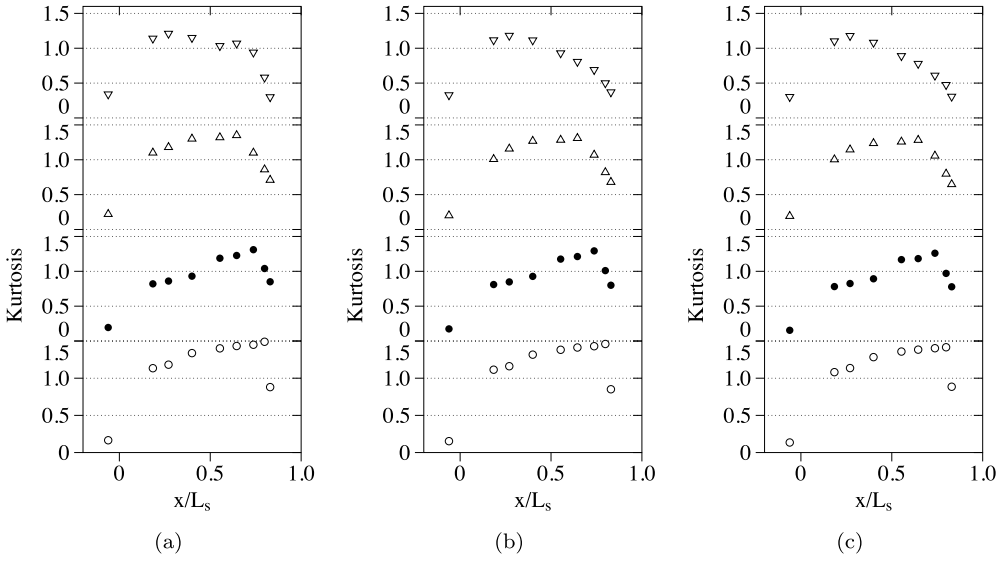

Fig. 9. Variation of the kurtosis versus the normalized distance in NWT for different steepnesses for m = (a) 1:25 (cases A1–A4); (b) 1:35 (cases B1–B4); (c) 1:45 (cases C1–C4). Open circles represent s = 0.0142; black circles for s = 0.0267; triangles for s = 0.0445; inverted triangles for s = 0.0623.

and $\beta = 0.54$ for case C4. Fig. 9 presents the distribution of the kurtosis along the wave tank (x/L_s) for (a) cases A1–A4 with m = 1:25, (b) cases B1–B4 with m = 1:35, and (c) cases C1–C4 with m = 1:45 (in the order of the lower to the upper symbols in Fig. 9). The changes in the skewness and kurtosis are mainly caused by the increasing contribution of the higher-frequency wave components during the wave propagation over the slope. The waves with a smaller value of s are relatively longer, and interact more with the slope (Herbers et al., 2002). The results are consistent with the findings reported by Goda (2010). For a given wave steepness, waves on a steeper slope have a slightly larger skewness and kurtosis compared to waves on a relatively milder slope. However, the incident wave steepness is found to be the major factor in estimating the skewness and kurtosis.

Fig. 10 presents the distribution of the normalized bandwidth ($\hat{\nu}$) over the distance along the wave tank (x/L_s) for (a) cases A1–A4 with m = 1:25, (b) cases B1–B4 with m = 1:35, and (c) cases C1–C4 with m = 1:45 (in the order of the lower to the upper symbols in Fig. 10). The bandwidth $\hat{\nu}$ is normalized with the spectral bandwidth measured at the wave gauge located closest to the wave generation. In general, the spectral bandwidth increases with wave shoaling, reaches its maximum value at the breaking point, and then decreases after breaking. For a given slope, the maximum $\hat{\nu}$ at breaking is larger for waves with a higher spectral wave steepness s. The value of $\hat{\nu}$ is 1.49 at the breaking point and reduces to 1.39 after breaking for case A4. For case A1, the value of $\hat{\nu}$ becomes 1.44 at the breaking point and reduces to 1.17 after breaking. For a given spectral wave steepness s, the bandwidth increase is slightly larger for steeper seabed slopes compared to milder slopes. The values of $\hat{\nu}$ for cases A4 (s = 0.0623, m = 1:25) and C4 (s = 0.0623, m = 1:45) are 1.49 and 1.42, respectively at breaking. It is also noticed from Fig. 10 that the bandwidth increase is higher for waves with larger values of s. The increase in the spectral bandwidth is due to the growth of the higher-frequency components and redistribution of energy across the wave spectrum via energy transfers as observed in Fig. 7. Therefore, the shoaling process leads to the widening of the wave spectrum (i.e. energy transfer from the peak region to other frequency components). After breaking, the spectral bandwidth is reduced mainly

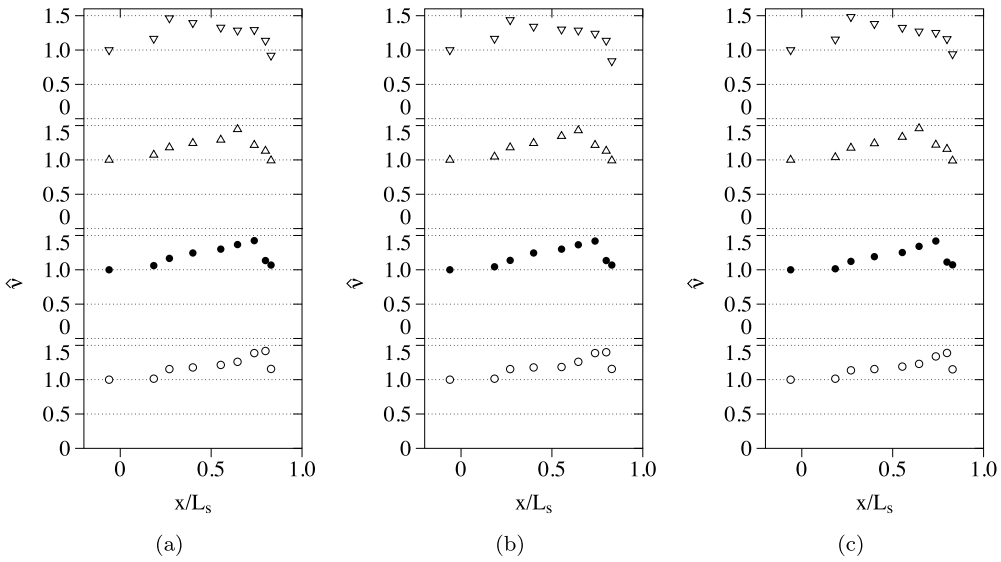

Fig. 10. Variation of the normalized bandwidth versus the normalized distance for different steepnesses for m = (a) 1:25 (cases A1–A4); (b) 1:35 (cases B1–B4); (c) 1:45 (cases C1–C4). Open circles represent s = 0.0142; black circles for s = 0.0267; triangles for s = 0.0445; inverted triangles for s = 0.0623.

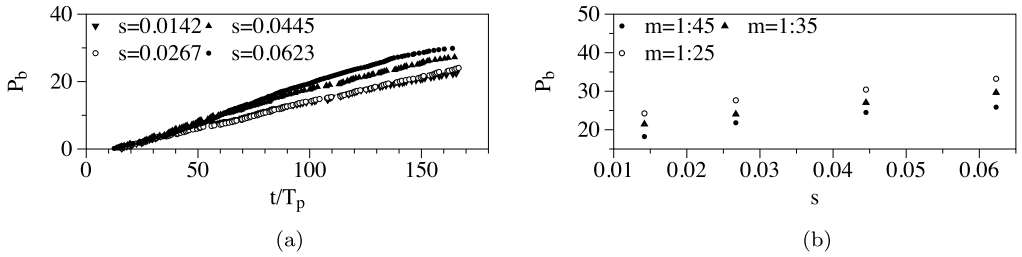

Fig. 11. Variation of the percentage of wave breaking P_b (a) versus the normalized simulation period t/T_p (m = 1:35, cases B1 to B4); (b) versus spectral wave steepness s for different seabed slopes.

due to the energy loss in the peak region during breaking. These observations are consistent with the results reported by Tian et al. (2011) for breaking focused waves.

3.3. Individual wave breaking

An irregular wave train is composed of regular wave components of different wave heights and periods. The geometric criteria based on the wave slope limit are used to determine breaking waves (Kjeldsen and Myrhaug, 1978; Bonmarin, 1989). The percentage of total number of breaking waves in a given irregular wave train including breaking at all locations P_b is defined as:

$$P_b = \frac{N_b}{N_i} \times 100 \tag{23}$$

where N_b is the total number of breaking waves in a given irregular wave train including breaking at all locations s and N_i is the total number of incident waves in a given irregular wave train.

Fig. 11a shows the percentage of total number of breaking waves in a given irregular wave train including breaking at all locations (P_b) versus the normalized simulation time (t/T_p) for a given seabed slope $m = 1:35$ (case B1 to B4), where t is the simulation time. It is observed from Fig. 11a that P_b for case B4 (s = 0.0623) has the highest value of 29%, while for case B1 (s = 0.0142) this value is 21%. The value of P_b is larger for the higher spectral wave steepness at each value of the normalized time step (t/T_p) for a given slope. However, the difference in P_b values until t/T_p = 50 for the different wave steepness cases is very small. The P_b value increases sharply after t/T_p = 50 for the wave spectra with the higher wave steepness (s = 0.0445 and 0.0623) in comparison to the low steepness cases. The early wave breaking is induced for the higher wave steepnesses; the individual waves possess higher incident wave heights and they break farther offshore. The waves with lower wave steepness undergo more wave shoaling and wave deformation, suggesting more onshore wave breaking. For the case with the largest spectral wave steepness (s) and steepest slope (m) (case A4), P_b is largest (38.9%), while for the case with the lowest s and lowest m (case C1), P_b is smallest (21.5%). Fig. 11b shows P_b versus s for different m. As expected, for a given steepness it appears that P_b is larger for the steeper slope.

3.4. Breaking wave characteristics

Fig. 12 presents the breaker depth index (γ_b) (Fig. 12a) and the breaker height index (Ω_b) (Fig. 12b) versus the surf similarity parameter at breaking (ξ_b) for cases A1 and C4. For case A1 (s = 0.0142, m = 1:25), it is observed that the values of γ_b and Ω_b decrease as ξ_b increases and most of the waves break as plunging breakers. When the slope is relatively steep (m = 1:25), the waves break farther offshore with lower H_b and with more reflections from the slope for ξ_b>0.4. An expected overall range as per the model given by Ostendorf and Madsen (1979) for γ_b is between 0.3 and 2.0. Most of the γ_b values are in this range as shown in Fig. 12a. The values lower than this range might indicate steepness-limited breaking due to wave-wave interactions such as overtaking and/or reflection, while the values higher than this range might be due to the coincidence of a reflected wave trough and an incident wave crest as it nears incipient breaking, which would shift the onset of breaking of the incident wave into shallower water. The low frequency waves propagate faster and experience more reflections from the slope (according to Battjes (1974), the reflection coefficient

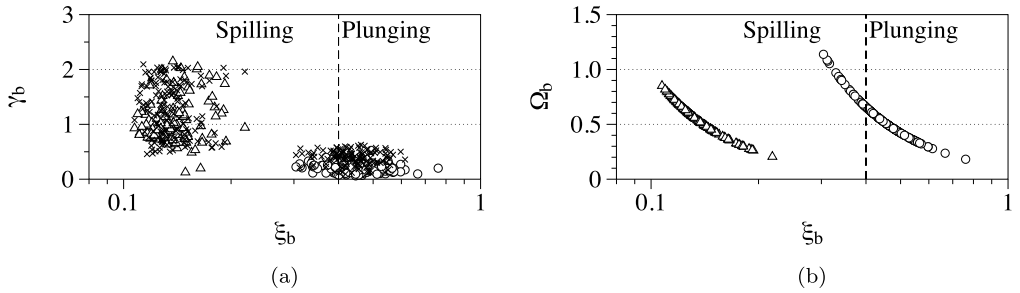

Fig. 12. Variation of the (a) breaker depth index γ_b; (b) breaker height index Ω_b versus the surf similarity parameter (logarithmic x-axis) at breaking ξ_b. Left side shows spilling breakers (case C4) and right side shows plunging breakers (case A1). Open circles represent case A1 (s = 0.0142, m = 1:25); triangles for case C4 (s = 0.0623, m = 1:45); crosses present results by using the model given by Ostendorf and Madsen (1979).

is directly proportional to ξ_b^2). The plunging breakers experience more reflections due to larger ξ_b^2. Only few waves have a value of more than 1 for Ω_b (case A1), which means that only few waves grow more than H_{so} during the shoaling process and have a breaking height H_b higher than H_{so} in the irregular wave train. For case C4 (s = 0.0623, m = 1:45), the trend of γ_b increases and Ω_b decreases as ξ_b increases. Here, all the waves break as spilling breakers and have values for Ω_b lower than 1, which means that none of the waves in the irregular wave train have a higher H_b than H_{so} during the shoaling process. The spilling breakers experience less reflections due to lower ξ_b^2. On a relatively milder slope, the waves break more onshore at shallower water depths and experience more deformation. The wave spectra with larger spectral wave steepness s on milder slopes undergo less deformation (Hajime and Kirby, 1992). Specifically, for the irregular wave train dominated by plunging breakers, the breaking is also affected by their interaction with the slope.

In order to investigate the statistics of the breaker indices, the cumulative distribution functions (CDF) for both breaker indices (γ_b and Ω_b) are analysed. Figs. 13 and 14 present the cumulative distribution functions (CDF) for the normalized breaker indices $\hat{\gamma}_b$ and $\hat{\Omega}_b$, respectively, for cases A1 and C4. The breaker indices are normalized with their corresponding rms values. Two different distributions: the Weibull distribution and the lognormal distribution, are tested. The lognormal probability density function (PDF) is given by:

$$p(x) = \frac{1}{x\sigma_l\sqrt{2\pi}} exp\{-\frac{(\ln x - \mu_l)^2}{2\sigma_l^2}\} \tag{24}$$

where μ_l and σ_l represent the log mean and log standard deviation of x, respectively; the best fit values of μ_l and σ_l for $\hat{\gamma}_b$ and $\hat{\Omega}_b$ are given in Table A.1.

The Weibull PDF is given by:

$$p(x) = \frac{b}{a}(\frac{x}{a})^{b-1} exp\{-(\frac{x}{a})^b\} \tag{25}$$

where b is the shape parameter and a is the scale parameter; the best fit values of a and b for $\hat{\gamma}_b$ and $\hat{\Omega}_b$ are presented in Table A.1.

Figs. 13a and 13b indicate that the lognormal distribution is more appropriate for the breaker depth index $\hat{\gamma}_b$ due to a better fit with the numerical data compared to the Weibull distribution for both cases: spilling and plunging breakers (cases C4 and A1). This is also obvious by comparing the log-likelihood (LL) values in Table A.1: *i.e.* , the LL values can be used to compare the best fit between two distributions. A relatively higher (or smaller negative) LL value gives a better distribution fit for the data (Kececioglu, 1993).

The normalized breaker height index ($\hat{\Omega}_b$) follows the trend similar to $\hat{\gamma}_b$ for case A1 (Fig. 14a). The lognormal distribution gives the best fit in case of the irregular wave train dominated by the plunging breakers (case A1). For case C4 (spilling breakers), the Weibull distribution is more appropriate as suggested by a better fit to the numerical data (Fig. 14b), see Table A.1.

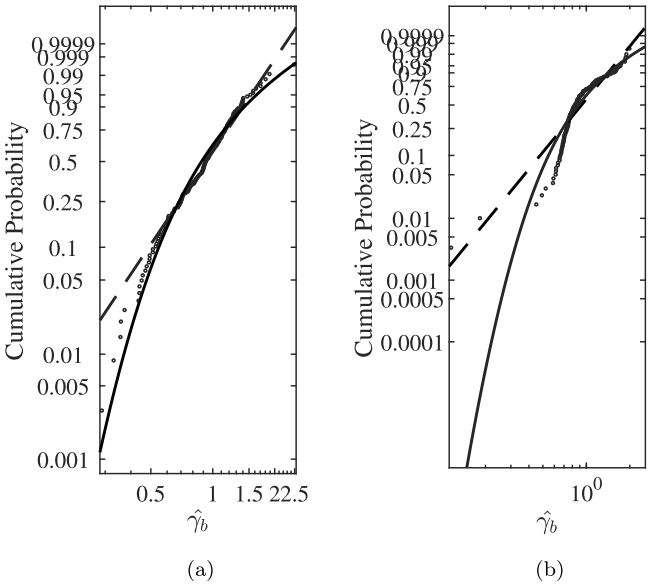

Fig. 13. CDF fits in the Weibull scale for the normalized breaker depth index $\hat{\gamma}_b$ for (a) case A1 (s = 0.0142, m = 1:25) (b) case C4 (s = 0.0623, m = 1:45). Black dots for numerical data; black dashed line for Weibull fit; solid black line for lognormal fit (for details of the CDF fits, see Table A.1 in Appendix).

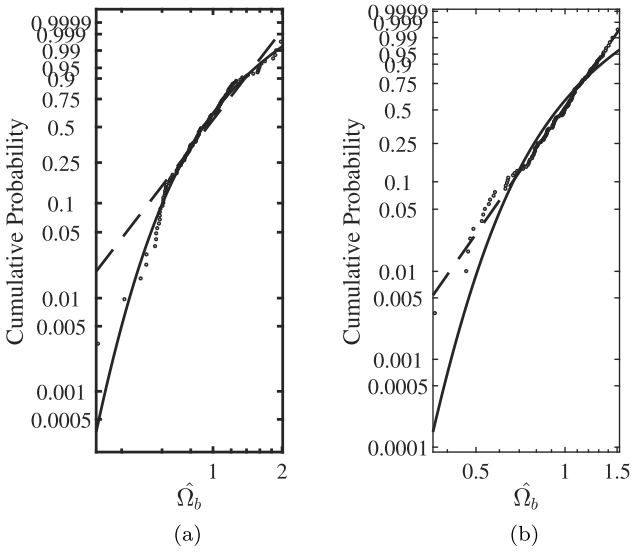

Fig. 14. CDF fits in the Weibull scale for the normalized breaker height index $\hat{\Omega}_b$ for (a) case A1 (s = 0.0142, m = 1:25); (b) case C4 (s = 0.0623, m = 1:45). Black dots for numerical data; black dashed line for Weibull fit; solid black line for lognormal fit (for details of the CDF fits, see Table A.1 in Appendix).

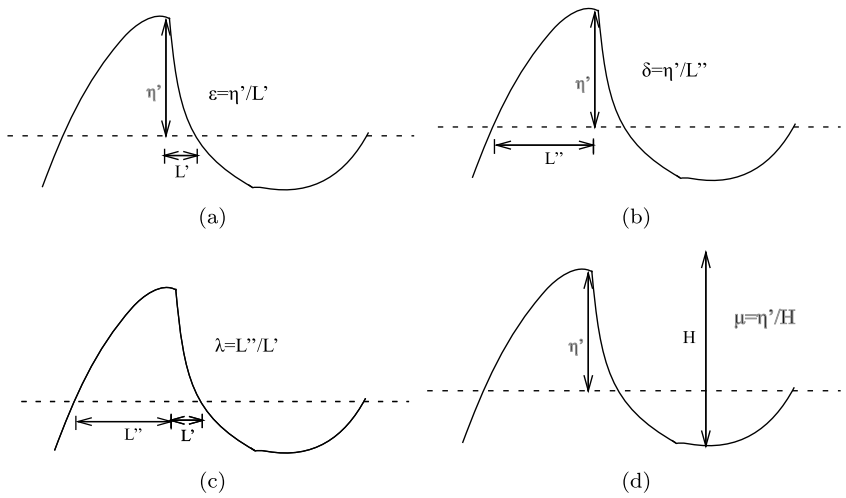

Fig. 15. Definitions of wave profile geometry (Kjeldsen and Myrhaug, 1978) (a) crest front wave steepness ε; (b) crest rear wave steepness δ; (c) vertical asymmetry factor λ; (d) horizontal asymmetry factor μ.

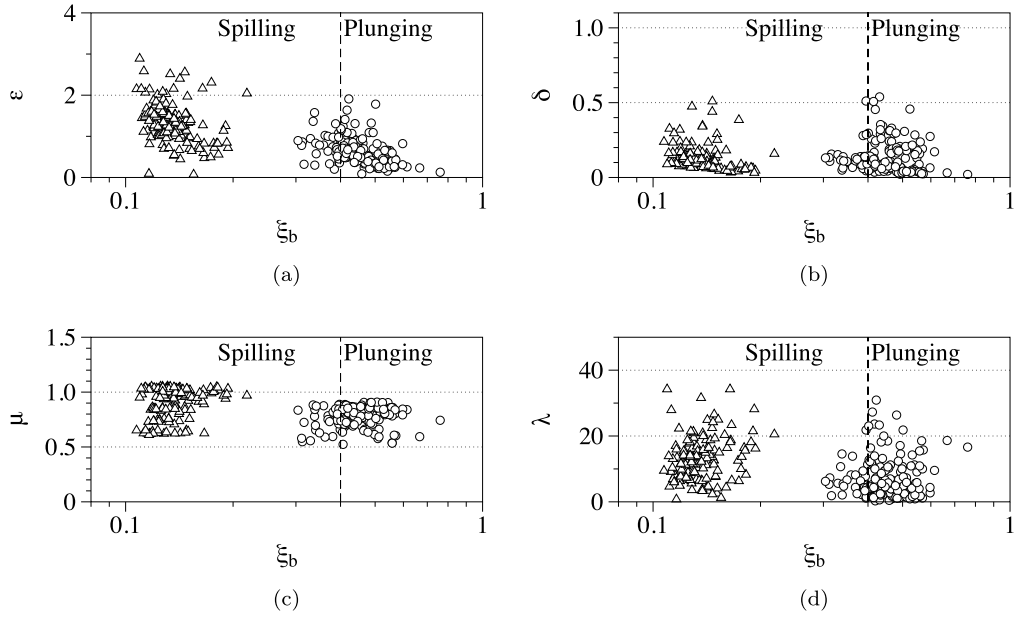

Fig. 16. Variation of the wave profile geometric properties versus the surf similarity parameter at breaking ξ_b (logarithmic x-axis) for cases A1 (s = 0.0142, m = 1:25) and case C4 (s = 0.0623, m = 1:45) (a) ε; (b) δ; (c) μ; (d) λ. Left side shows spilling breakers (case C4) and right side shows plunging breakers (case A1). Open circles represent case A1 (s = 0.0142, m = 1:25); triangles for case C4 (s = 0.0623, m = 1:45).

3.5. Geometric properties of wave profile at breaking

During the breaking process, the waves become more steep and asymmetric. The present study further investigates the geometric properties of the wave profile at breaking by using the steepness and asymmetry parameters (Fig. 15) defined by Kjeldsen and Myrhaug (1978).

3.5.1. Study of the breaker shape with the surf similarity parameter at breaking

The variation of different steepness and asymmetry parameters of the wave crest with the surf similarity parameter at breaking (ξ_b) is investigated here. Figs. 16a, 16b, 16c and 16d present the crest front wave steepness (ε), the crest rear wave steepness (δ), the horizontal asymmetry factor (μ) and the vertical asymmetry factor (λ), respectively, versus the surf similarity parameter at breaking (ξ_b) for cases A1 and C4. The crest front steepness (ε) values decrease in general, as ξ_b increases for both cases A1 and C4 (Figs. 16a and 16b). The values of ε for case C4 are slightly larger as compared to case A1, which is dominated by plunging breakers. The crest rear steepness (δ) decrease slightly as ξ_b increases for both, case A1 (dominated by plunging breakers) and case C4 (spilling breakers). The present findings are consistent with the results for breaking regular waves over slopes by Alagan Chella et al. (2015). However, some scatter is observed in the values of the breaker shape parameters. This could be due to wave–wave interactions and the superimposition of the reflected waves with the incident waves. The wave crest becomes more steep and skewed when the irregular wave train propagates over milder slopes (for spilling breakers) compared to steeper slopes (for plunging breakers). The low frequency waves (long waves) propagate faster and undergo more deformation. In case of the high frequency (shorter waves) waves, they interact less with the slope and the wave crest becomes relatively less deformed. The present results further confirm the findings for spilling breakers by Lader (2002).

It is noticed from Figs. 16c and 16d that μ and λ increase slightly as ξ_b increases for both cases A1 and C4. For the spilling breaker, the

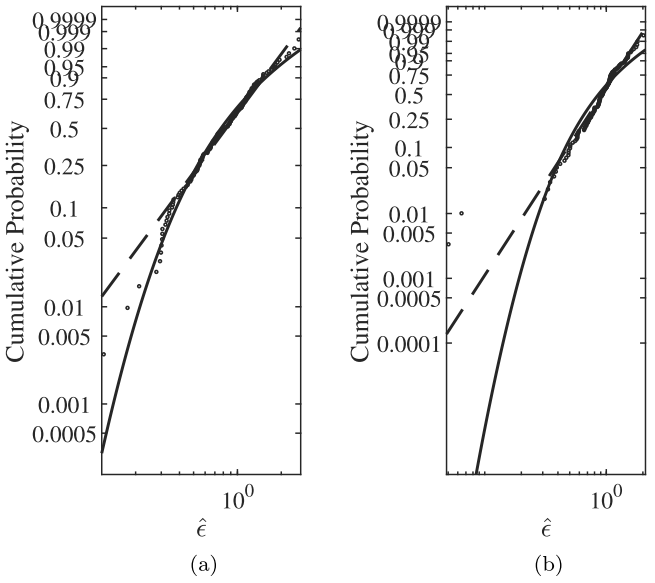

Fig. 17. CDF fits in the Weibull scale for the normalized crest front steepness $\hat{\epsilon}$ for (a) case A1 (s = 0.0142, m = 1:25); (b) case C4 (s = 0.0623, m = 1:45). Black dots for numerical data; black dashed line for Weibull fit; solid black line for lognormal fit (for details of the CDF fits, see Table A.1 in Appendix).

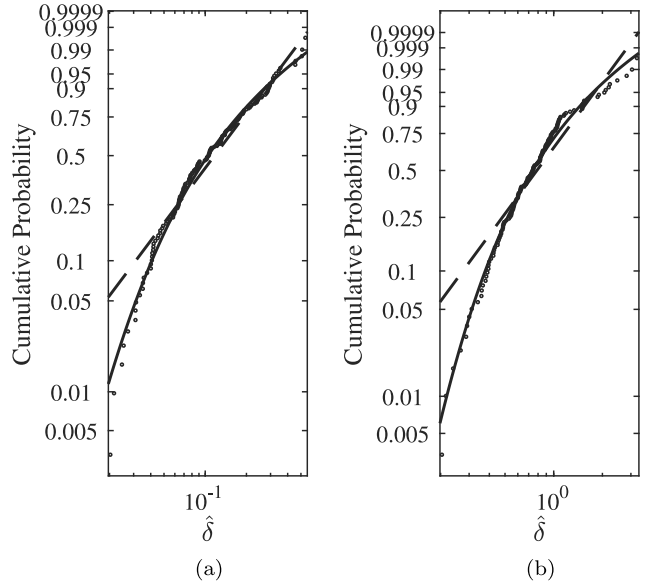

Fig. 18. CDF fits in the Weibull scale for the normalized crest rear steepness $\hat{\delta}$ for (a) case A1 (s = 0.0142, m = 1:25); (b) case C4 (s = 0.0623, m = 1:45). Black dots for numerical data; black dashed line for Weibull fit; solid black line for lognormal fit (for details of the CDF fits, see Table A.1 in Appendix).

front and rear faces of the wave crest become steeper with a gradual slight increase of the vertical asymmetry, and the forward wave trough flattens at wave breaking. For the plunging breaker, the front face of the wave crest becomes very steep without much change in the rear face of the wave crest due to more offshore wave breaking and undergoes less deformation.

3.5.2. Statistics for breaker shape parameters

Figs. 17 and 18 present the CDFs for the normalized crest front steepness ($\hat{\epsilon}$) and the normalized crest rear steepness ($\hat{\delta}$) for cases A1 and C4, i.e. ϵ and δ are normalized with their rms values ϵ_{rms} and δ_{rms}, respectively. Figs. 17a and 17b indicate that the lognormal distribution

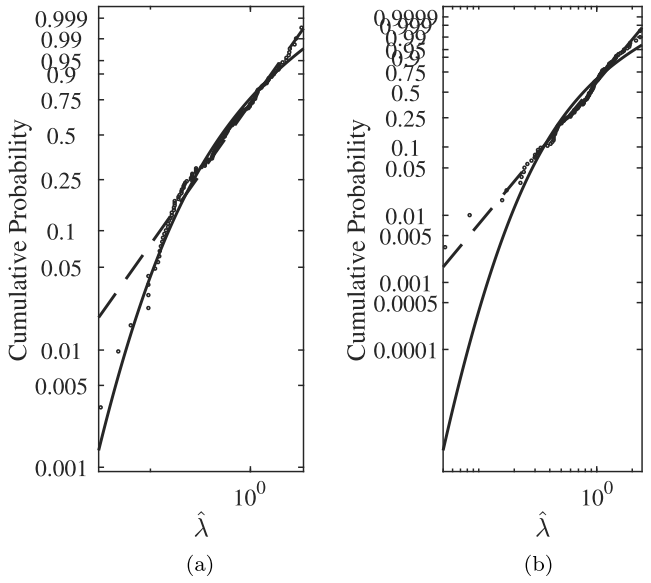

Fig. 19. CDF fits in the Weibull scale for the normalized vertical asymmetry factor $\hat{\lambda}$ for (a) case A1 (s = 0.0142, m = 1:25); (b) case C4 (s = 0.0623, m = 1:45). Black dots for numerical data; black dashed line for Weibull fit; solid black line for lognormal fit (for details of the CDF fits, see Table A.1 in Appendix).

Table 2
Significance of wave crest parameters with respect to the sea state (Myrhaug and Kjeldsen, 1984, 1986).

Wave crest geometry parameters	Wave height	Sea state
High	Low	Choppy sea
Low	High	Heavy swell
High	High	Rough sea with breaking waves

gives the best fit for $\hat{\epsilon}$ for cases A1 and the Weibull distribution is better suited for case C4 (spilling breaker, the Weibull and lognormal parameters as well as the LL values for $\hat{\epsilon}$ and $\hat{\delta}$ are given in Table A.1). For the crest rear steepness ($\hat{\delta}$), the lognormal distribution is more appropriate and fits the numerical data in a satisfactory manner for both cases A1 and C4 as observed in Fig. 18. Myrhaug and Kjeldsen (1984) reported that the Weibull distribution is the best fit for the normalized crest front steepness for the given field data in deep water. This suggests that the crest front steepness follows different distributions in deep and shallow water which can be attributed to the wave transformations originated by the changing water depths close to the coasts.

Fig. 19 presents the CDFs for the normalized vertical asymmetry factor ($\hat{\lambda}$) for cases A1 and C4, where λ is normalized with the rms value λ_{rms}. The lognormal distribution is better suited for $\hat{\lambda}$ for case A1 (plunging breaker) and the Weibull distribution is better suited for case C4 (spilling breaker) as seen in Fig. 19. For the normalized horizontal asymmetry factor ($\hat{\mu}$), none of the distributions give a good fit. Therefore, the figures are not presented here. Myrhaug and Kjeldsen (1984) reported that the lognormal distribution gives the best fit for the normalized vertical asymmetry factor for deep water waves measured in the field. According to Peregrine et al. (1980), the water accelerations exceed the acceleration of gravity (g) in a thin region on the front face of the wave (up to about 5 g) in the subsequent development of the overturning wave crest. The region on and beneath the rear slope of the wave has low fluid accelerations. This region ensures that the high pressure gradients and wave asymmetry required to produce the acceleration near the wave crest front can exist. The wave crest and asymmetry parameters in combination with the breaker indices (which gives information about H_b and d_b) are important in describing the rough sea state. They can further be used to assess the probability of occurrence of steep and asymmetric waves in shallow water. The

Table A.1
Table listing the details for different statistical parameters for the Weibull and lognormal distributions.

	Distribution	Parameters	Case A1	Case C4
Normalized breaker depth index $\hat{\gamma}_b$	Weibull	a	1.05	1.05
		b	2.93	2.85
		LL	−55.4	−49.4
	Lognormal	μ_l	−0.12	−0.12
		σ_l	0.37	0.37
		LL	−52.5	−44.8
Normalized breaker height index $\hat{\Omega}_b$	Weibull	a	1.06	1.06
		b	3.20	4.80
		LL	−37.5	7.2
	Lognormal	μ_l	−0.10	−0.06
		σ_l	0.31	0.26
		LL	−25.9	−5.4
Normalized crest front wave steepness $\hat{\varepsilon}$	Weibull	a	0.99	1.04
		b	2.07	2.89
		LL	−87.5	−53.8
	Lognormal	μ_l	−0.26	−0.15
		σ_l	0.55	0.49
		LL	−85.8	−80.9
Normalized crest rear wave steepness $\hat{\delta}$	Weibull	a	0.15	0.97
		b	1.42	1.79
		LL	163.4	−88.8
	Lognormal	μ_l	−2.26	−0.30
		σ_l	0.74	0.52
		LL	176.4	−69.5
Normalized vertical asymmetry factor $\hat{\lambda}$	Weibull	a	0.80	1.01
		b	1.31	2.12
		LL	106.85	−83.75
	Lognormal	μ_l	−0.67	−0.26
		σ_l	0.95	0.60
		LL	−106.2	−97.9

different combinations of the wave crest parameters suggest different sea states (Table 2) (Myrhaug and Kjeldsen, 1984, 1986). It could be important for the coastal and naval engineers for the performance and reliability analysis of coastal structures and ships under severe sea conditions (Ploeg, 1982).

4. Conclusions

A two-phase CFD model is used to investigate some unexplored aspects of breaking irregular waves over sloping seabeds. The numerical model is first validated for modelling of breaking irregular waves over a submerged bar by comparing with the Beji and Battjes (1993) experimental data at different wave gauge locations along the wave tank during the complex wave transformation processes involving wave shoaling and wave breaking.

An extensive numerical analysis is performed to study breaking irregular waves over slopes using the setup similar to Ting and Kirby (1996). The investigation is carried out for multiple incident irregular wave trains propagating over different slopes. The wave breaking process is initiated by an increase of wave crest height which is followed by an overturning motion of the jet, resulting in the downward directed motion of the water jet with an enclosed air pocket. First, the energy transfer from the spectral peak region towards higher-frequencies is investigated and its role in influencing the free surface elevation skewness and spectral bandwidth during wave shoaling and wave breaking processes is also highlighted. The incident wave parameters and sloping sea bed play major roles in affecting the breaking wave characteristics and wave crest geometric parameters. The wave crest deformation is mainly affected by the length and steepness of the slope. The waves with larger incident wave steepness undergo less deformation due to farther offshore wave breaking at larger water depths. Further, cumulative distribution fits are estimated for breaker indices and wave crest geometric parameters. The following conclusions can be drawn from the study:

- As expected, the percentage of breaking waves in the irregular wave train increases as the spectral wave steepness or the steepness of the slope over which the waves are propagating increases; 39% of the wave components in the steepest incident irregular wave train (s = 0.0623) break during the propagation over the steepest slope (m = 1:25). Most of these waves break farther offshore at larger water depths.
- The non-linear energy transfer from the spectral peak region (f/f_p = 0.9–1.1) to the above peak region (f/f_p = 1.2–1.5) and higher-frequency region (f/f_p = 1.5–2.5) during the wave transformation process governs the changes in free surface elevation skewness and spectral bandwidth. The waves with lower incident spectral wave steepness tend to have a higher skewness value after breaking. The bandwidth of the wave spectrum increases until wave breaking and decreases after breaking. The bandwidth is mainly affected by the incident irregular wave parameters rather than the seabed slope.
- For a steeper seabed slope (m = 1:25), most of the waves in the wave spectrum with the lower spectral wave steepness break as plunging breakers. For the wave spectrum with a higher spectral wave steepness propagating over milder slopes (m = 1:45), the number of waves breaking as spilling breakers increases.
- For the irregular waves with a lower spectral wave steepness (s = 0.0267) propagating over a steep seabed slope (m = 1:25), few waves in the irregular wave train exceed H_{so} during the shoaling process and have a breaking height H_b higher than H_{so}. For the incident wave spectrum with a larger spectral steepness (s = 0.0623) over a milder slope (m = 1:45), none of the waves in the irregular wave train have a higher H_b than H_{so} during the shoaling process. The Weibull and lognormal distributions can be used to predict the statistics of the breaker height and the breaker depth indices, respectively.
- The crest front wave and crest rear wave steepnesses decrease as the surf similarity parameter increases at breaking. The steepness

of the forward face of the wave crest increases as the waves approach the shore. The wave crest becomes more steep and skewed when the irregular wave train propagates over milder slopes (for spilling breakers) as compared to steeper slopes (for plunging breakers). The low frequency waves (long waves) propagate faster and undergo more deformation. In case of the high frequency (shorter) waves, they interact less with the slope and the wave crest becomes relatively less deformed. In general, the lognormal distribution is suitable for determining the statistics of wave steepness and asymmetry factors.

CRediT authorship contribution statement

Ankit Aggarwal: Conceptualization, Simulations, Analysis of results, Manuscript writing. **Mayilvahanan Alagan Chella:** Conceptualization support, Proof reading the manuscript. **Hans Bihs:** Proof reading the manuscript, Supervising the work, Contribution with the numerical code. **Dag Myrhaug:** Proof reading the manuscript, Supervising the work.

Declaration of competing interest

The authors declare that they have no known competing financial interests or personal relationships that could have appeared to influence the work reported in this paper.

Acknowledgements

The research work has been funded by the Research Council of Norway through the project "Hydrodynamic Loads on Offshore Wind Turbine Substructures" (project number: 246810). The authors gratefully acknowledge the computing time granted by NOTUR, Norway (project number: NN2620k).

Appendix. Table listing the details of the CDF fits

See Table A.1.

References

Afzal, M.S., Bihs, H., Kamath, A., Arntsen, Ø.A., 2015. Three-dimensional numerical modeling of pier scour under current and waves using level-set method. J. Offshore Mech. Arct. Eng. 137 (3), 032001.

Afzal, M.S., Bihs, H., Kumar, L., 2020. Computational fluid dynamics modeling of abutment scour under steady current using the level set method. Int. J. Sediment Res. 35 (4), 355–364.

Aggarwal, A., Bihs, H., Myrhaug, D., Chella, M.A., 2019a. Characteristics of breaking irregular wave forces on a monopile. Appl. Ocean Res. 90, 101846.

Aggarwal, A., Bihs, H., Shirinov, S., Myrhaug, D., 2019b. Estimation of breaking wave properties and their interaction with a jacket structure. J. Fluids Struct. 91, 102722.

Aggarwal, A., Tomaselli, P.D., Christensen, E.D., Bihs, H., 2020. Computational fluid dynamics investigations of breaking focused wave-induced loads on a monopile and the effect of breaker location. J. Offshore Mech. Arct. Eng. 142 (2), 021903.

Alagan Chella, M., Bihs, H., Myrhaug, D., Michael, M., 2015. Breaking characteristics and geometric properties of spilling breakers over slopes. Coast. Eng. 95, 4–19.

Alagan Chella, M., Bihs, H., Myrhaug, D., Michael, M., 2016. Hydrodynamic characteristics and geometric properties of plunging and spilling breakers over impermeable slopes. Ocean Model. 103, 53–72.

Battjes, J.A., 1974. Surf similarity. In: Proceedings of the 14th International Conference Coastal Engineering. American Society of Civil Engineers, New York, pp. 466–480.

Beji, S., Battjes, J., 1993. Experimental investigation of wave propagation over a bar. Coast. Eng. 19, 151–162.

Bihs, H., Kamath, A., 2017. A combined level set/ghost cell immersed boundary representation for floating body simulations. Internat. J. Numer. Methods Fluids 83 (12), 905–916.

Bihs, H., Kamath, A., Alagan Chella, M., Aggarwal, A., Arntsen, A.Ø., 2016. A new level set numerical wave tank with improved density interpolation for complex wave hydrodynamics. Comput. & Fluids 140, 191–208.

Bonmarin, P., 1989. Geometric properties of deep water breaking waves. J. Fluid Mech. 209, 405–433.

Bradford, F., 2000. Numerical simulation of surf zone dynamics. J. Ports Coast. Waterw. Ocean Eng. 126, 1–13.

Camenen, B., Larson, M., 2007. Predictive formulas for breaker depth index and breaker type. J. Coast. Res. 1028–1041.

Chen, G., Kharif, C., Zaleski, S., Li, J., 1999. Three-dimensional Navier- Stokes simulation of breaking waves. Phys. Fluids 11, 121–133.

Chorin, A.J., 1968. Numerical solution of the Navier-Stokes equations. Math. Comp. 22, 745–762.

Christensen, E.D., 2006. LES simulation of spilling and plunging breakers. Coast. Eng. 53, 463–485.

Dalzell, J.F., 1999. A note on finite depth second-order wave–wave interactions. Appl. Ocean Res. 21, 105–111.

Durbin, P., 2009. Limiters and wall treatments in applied turbulence modeling. Fluid Dyn. Res. 41 (1), 012203.

Falgout, R.D., Yang, U.M., 2002. HYPRE: A library of high performance preconditioners. In: Sloot, P.M.A., Hoekstra, A.G., Tan, C.J.K., Dongarra, J.J. (Eds.), Computational Science — ICCS 2002: International Conference Amsterdam, the Netherlands, April 21–24, 2002 Proceedings, Part III. Springer Berlin Heidelberg, pp. 632–641.

Garcia, N., Lara, L.J., Losada, I., 2004. 2-d numerical analysis of near-field flow at low-crested permeable breakwaters. Coast. Eng. 51, 991–1020.

Goda, Y., 1970. A synthesis of breaker indices. Japan. Soc. Civ. Eng. 227–230.

Goda, Y., 2010. Reanalysis of regular and random breaking wave statistics. Coast. Eng. 52, 71–106.

Griebel, M., Dornseifer, T., Neunhoeffer, T., 1998. Numerical Simulations in Fluid Dynamics. SIAM.

Hajime, M., Kirby, T.J., 1992. Hybrid frequency-domain KdV equation for random wave transformation. Phil. Trans.: Math. Phys. Eng. Sci. 354 (1707), 649–676.

Hasselmann, D.E., Dunckel, M., Ewing, A.J., 1980. Directional wave spectra observed during JONSWAP 1973. J. Phys. Oceanogr. 10 (8), 1264–1280.

Herbers, T., Elgar, N., Sarap, A., Guza, A., 2002. Nonlinear dispersion of surface gravity waves in shallow water. J. Phys. Oceanogr. 32, 1181–1193.

Hieu, D., Katsutoshi, T., Ca, T.V., 2004. Numerical simulation of breaking waves using a two-phase flow model. Appl. Math. Modelling 28, 983–1005.

Hwang, P.A., 1984. Profile asymmetry of shoaling waves on a mild slope. In: 19th Coastal Engineering Proceedings. pp. 1016–1027.

Jiang, J., Shu, C.W., 1996. Efficient implementation of weighted ENO schemes. J. Comput. Phys. 126, 202–228.

Kamath, A., Alagan Chella, M., Bihs, H., Arntsen., A.Ø., 2017. Energy transfer due to shoaling and decomposition of breaking and non-breaking waves over a submerged bar. Eng. Appl. Comput. Fluid Mech. 11 (1), 450–466.

Kececioglu, D., 1993. Reliability and Life Testing Handbook. Prentice Hall.

Kjeldsen, S.P., Myrhaug, D., 1978. Kinematics and Dynamics of Breaking Waves. Technical Report, River and Harbour Laboratory. The Norwegian Institute of Technology, Trondheim, Norway, STF60A78100.

Lader, P.F., 2002. Geometry and Kinematics of Breaking Waves (Ph.D. thesis). Department of Marine Technology, NTNU.

Lara, J., Losada, I., Liu, P.-F., 2006. Breaking waves over a mild gravel slope: experimental and numerical analysis. J. Geophys. Res. 111, C11019.

Lin, P., Liu, L., 1998. A numerical study of breaking waves in the surf zone. J. Fluid Mech. 359, 239–264.

Liu, P., 2000. Wavelet transform and new prospective on coastal and ocean engineering data analysis. Adv. Coast. Ocean Eng. 6, 57–101.

Longuet-Higgins, M.S., 1975. On the joint distribution of the periods and amplitudes of sea waves. J. Geophys. Res. 80, 2688–2693.

Longuet-Higgins, M.S., Cokelet, E.D., 1976. The deformation of steep surface waves on water 1. a numerical method of computation. Proc. R. Soc. Lond. 350, 1–26.

Lubin, P., Vincent, S., Abadie, S., Caltagrione, J., 2006. Three-dimensional LES simulation of air entrainment under plunging breaking waves. Coast. Eng. 53, 631–655.

Mayer, S., Garapon, A., Sørensen, S.L., 1998. A fractional step method for unsteady free surface flow with applications to non-linear wave dynamics. Int. J. Numer. Math. Fluids 28, 293–315.

Mori, N., Yasuda, T., 1994. Orthonormal wavelet analysis for deep-water breaking waves.. In: 24th Proceedings of the International Conference in Coastal Engineering. pp. 412–426.

Myrhaug, D., Kjeldsen, S.P., 1984. Parametric modelling of joint probability density distributions for steepness and asymmetry in deep water waves. Appl. Ocean Res. 6 (4), 207–220.

Myrhaug, D., Kjeldsen, S.P., 1986. Steepness and asymmetry of extreme waves and the highest waves in deep water. Ocean Eng. 6 (13), 549–568.

Ochi, M., Passiliao, E., Malakar, S., 1996. Joint Probability Distribution of the Average Period and Significant Height. University of Florida Repository.

Ong, M.C., Kamath, A., Bihs, H., Afzal, M.S., 2017. Numerical simulation of free-surface waves past two semi-submerged horizontal circular cylinders in tandem. Mar. Struct. 52, 1–14.

Osher, S., Sethian, J.A., 1988. Fronts propagating with curvature- dependent speed: Algorithms based on hamilton-jacobi formulations. J. Comput. Phys. 79, 12–49.

Ostendorf, D.W., Madsen, O.S., 1979. An Analysis of Longshore Currents and Associated Sediment Transport in the Surf Zone. Report no: MITSG79-13, MIT repository.

Paulsen, T.B., Bredmose, H., Bingham, B.H., Schloer, S., 2013. Steep wave loads from irregular waves on an offshore wind turbine foundation: computation and experiment. In: 32nd Proceedings of the ASME International Conference on Ocean, Offshore & Arctic Engineering.

Peregrine, D.B., Cokelet, E.D., Mclever, P., 1980. The fluid mechanics of waves approaching breaking. 17th Proceedings of the International Conference in Coastal Engineering, pp. 512–528.

Ploeg, J., 1982. Working group on wave generation and analysis of the section on maritime hydraulics. J. Hydraul. Res. 20 (5), 393–394.

Seyama, A., Kimura, A., 1988. The measured properties of irregular wave breaking and wave height change after breaking on the slope. Coast. Eng. 21, 419–432.

Shu, C.W., Oscher, S., 1988. Efficient implementation of essentially non-oscillatory shock capturing schemes II. J. Comput. Phys. 77, 439–471.

Thorpe, S., Humphries, P., 1980. Bubbles and breaking waves. Nature 283, 463–465.

Tian, Z., Perlin, M., Choi, W., 2011. Frequency spectra evolution of two-dimensional focusing wave groups in finite depth water. J. Fluid Mech. 688, 169–194.

Ting, F., 2001. Laboratory study of wave and turbulence velocities in a broad-banded irregular wave surf zone. Coast. Eng. 43, 183–208.

Ting, F., Kirby, J.T., 1996. Dynamics of surf-zone turbulence in a spilling breaker. Coast. Eng. 27, 131–160.

Van Loco, J., Elskens, M., Croux, C., 2002. Linearity of calibration curves: use and misuse of the correlation coefficient. Accred. Qual. Assur. 7, 281–285.

Watson, K.M., West, B.J., 1975. A transport-equation description of nonlinear ocean surface wave interactions. J. Fluid Mech. 70, 815–826.

Weggel, R.J., 1972. Maximum breaker height. J. Waterw. Harbors Coast. Eng. Div. 98.

Wilcox, D., 1994. Turbulence Modeling for CFD. DCW Industries Inc., La Canada, California.